Acta Materialia 212 (2021) 116876

Contents lists available at ScienceDirect

Acta Materialia

journal homepage: www.elsevier.com/locate/actamat

Full length article

Unique crystallographic texture formation in Inconel 718 by laser powder bed fusion and its effect on mechanical anisotropy

Ozkan Gokcekaya[a,b,1], Takuya Ishimoto[a,b,1], Shinya Hibino[a,c], Jumpei Yasutomi[a], Takayuki Narushima[d], Takayoshi Nakano[a,b,*]

[a] Division of Materials and Manufacturing Science, Graduate School of Engineering, Osaka University, 2-1, Yamadaoka, Suita, Osaka 565-0871, Japan
[b] Anisotropic Design & Additive Manufacturing Research Center, Osaka University, 2-1, Yamadaoka, Suita, Osaka 565-0871, Japan
[c] Technical Institute, Corporate Technology Division, Kawasaki Heavy Industries, Ltd., 1-1, Kawasaki-cho, Akashi 673-8666, Japan
[d] Department of Materials Processing, Graduate School of Engineering, Tohoku University, 6-6-02 Aza Aoba, Aramaki, Aoba-ku, Sendai 980-8579, Japan

ARTICLE INFO

Article history:
Received 25 November 2020
Revised 12 March 2021
Accepted 4 April 2021
Available online 21 April 2021

Keywords:
Laser powder bed fusion
Inconel 718
Crystallographic texture
Lamellae
Mechanical anisotropy

ABSTRACT

Additive manufacturing offers an exclusive way of anisotropic microstructure control with a high degree of freedom regarding variation in process parameters. This study demonstrates a unique texture formation in Inconel 718 (IN718) using a bidirectional laser scan in a laser powder bed fusion (LPBF) process for tailoring the mechanical properties. We developed three distinctive textures in IN718 using LPBF: a single-crystal-like microstructure (SCM) with a <110> orientation in the build direction (BD), crystallographic lamellar microstructure (CLM) with a <110>-oriented main layer and <100>-oriented sub-layer in the BD, and polycrystalline with a weak orientation. The microstructure observations and finite element simulations showed that the texture evolution of the SCM and CLM was dominated by the melt-pool shape and related heat-flow direction. The specimen with CLM exhibited a simultaneous improvement in strength and ductility owing to the stress-transfer coefficient between the <110>-oriented main and <100>-oriented sub-grains, showing superior mechanical properties compared to cast-IN718. This behavior is largely attributed to the presence of the boundary between the main and sub-layers (crystallographic grain boundary) lying parallel to the BD uniquely formed under the LPBF process. Furthermore, the strength–ductility balance of the part with the CLM can be controlled by changing the stress-transfer coefficient and the Schmidt factor through an alteration of the loading axis. Control of the crystallographic texture, including the CLM formation, is beneficial for tailoring and improving the mechanical performance of the structural materials, which can be a promising methodology.

1. Introduction

In recent years, along with the development of additive manufacturing (AM) technology, laser powder bed fusion (LPBF) has become an important means of forming complex components owing to its high-performance entity-free formation process, allowing the production of challenging pure metals and various alloys [1–3]. Unlike a traditional casting method, the melt pool in LPBF can be identified with a high thermal gradient and rapid cooling rate (~10^6 K/s) up to ambient temperature [4]; thus, elemental segregation is greatly suppressed while an increase in dislocations is favored [5]. It is commonly accepted that LPBF-build parts experience a layer-wise cyclic thermal history [6], which makes the microstructure of the material different from that obtained through traditional processing methods.

Previous investigations have shown that the process parameters of the LPBF, such as the scanning speed [7], hatch spacing [7], laser energy density [8], build orientation [6], and scanning strategy [9,10], affect the microstructure [11] and density of the parts [12], and the magnitude and distribution of the residual stress [13], eventually leading to different mechanical properties of the as-built parts [14,15]. However, the strength anisotropy is more dependent on the grain texture, particularly when a strong texture coexists with the directional grain morphology [16].

Nickel-based superalloys have a broad range of applications in the aerospace, automotive, and energy industries, and Inconel 718 (IN718) superalloys have been widely used in nuclear reactors, aircraft engines, and other high-temperature applications owing to

* Corresponding author at: Division of Materials and Manufacturing Science, Graduate School of Engineering, Osaka University, 2-1, Yamadaoka, Suita, Osaka 565-0871, Japan.
E-mail address: nakano@mat.eng.osaka-u.ac.jp (T. Nakano).
[1] These authors contributed equally to this work.

https://doi.org/10.1016/j.actamat.2021.116876

their high strength, creep resistance, good corrosion resistance, and long fatigue life at elevated temperatures [17,18]. IN718 has a face-centered cubic (FCC) crystalline structure with an easy-growth direction of <100>, which results in grains preferentially growing with a <100> direction more closely aligned to the heat-flow direction [19]. By changing the process parameters in LPBF, the heat-flow direction as well as the balance between the thermal gradient (G) and solidification rate (R) can be locally changed [20], resulting in the evolution of various grain morphologies and crystallographic textures from equiaxed to columnar microstructures [20,21]. Inspired by the various crystallographic textures [14,15,22–27] and grain morphologies achieved through different process parameters in LPBF, microstructural control within the LPBF-build parts is key to property enhancement. The heat-flow direction and thermal gradient-solidification rate balance were determined by the energy input into the material.

The energy input in AM can be quantified by the energy density [28], which is defined as a function of the laser power, scan speed, layer thickness, and hatch spacing [29]. Several researchers [25,26,30] have shown the impact of energy density on the microstructure, porosity, and mechanical properties of the AM components because it determines the heating/cooling rate, thermal dynamic behavior, and shape of the melt pool. A graded IN718 was fabricated using LPBF with different energy densities [31], resulting in a strongly textured microstructure with elongated <100> grains with a high energy input. A study on high-silicon steel fabricated using LPBF suggested that a <100> fiber texture can be altered into a cubic texture when the shape of the melt pool is changed from shallow into deep with an increased energy density by decreasing the scan speed [22]. It is assumed that the appearance of deeper melt pools with a solidification front almost horizontal at the melt pool centerlines induces two easy-growth directions perpendicular to each other from the melt pool sides and center, which form a <100> cubic texture.

In addition to the common <100> texture obtained through LPBF, a few recent studies attained a <110> crystallographic texture along the build direction (BD) for an FCC crystal structure [23–26]. McLouth et al. reported a transition of a <100> texture to a <110> texture with a defocused laser beam, which altered the melt pool shape and resulted in excellent high-temperature creep properties [24]. Sun et al. investigated the difference in strengthening mechanism of <100> and <110> textured 316L stainless steel fabricated using LPBF, in which the <100> textured microstructure deformed through a dislocation slip mechanism while the <110> oriented grains exhibited deformation twinning and a simultaneous strength and ductility improvement [23]. It has been well recognized that the primary strengthening mechanism operated in cast-IN718 is the precipitation of a coherent ordered γ" phase [32]. However, Sun et al. reported a unique lamellar crystallographic orientation of 316L with excellent mechanical properties, which surpassed the mechanical properties of the <110> oriented single-crystal like microstructure and as-cast 316L [25]. Ishimoto et al. evaluated the formation of this unique lamellar microstructure in 316L alternately oriented as <110> main and <100> sub-texture formations owing to the differences in melt pool shape induced by the energy input [26]. To the best of our knowledge, there have been no studies focusing on the <110> crystallographic orientation of IN718 as a single-crystal-like microstructure or crystallographic lamellar texture formation.

This study aims to overcome the trade-off between strength and ductility in LPBF-built components through in situ tailoring of specific crystallographic textures and grain orientations. The unique texture formation in IN718 fabricated by LPBF with a bidirectional scan strategy was investigated for the first time to generate a <110>//BD-oriented single-crystal-like microstructure (SCM), a crystallographic lamellar microstructure (CLM) [25], which is composed of <110>//BD-oriented main grains and <100>//BD-oriented sub-grains, and a polycrystalline microstructure (PCM) by changing the laser power and scan speed. To discuss the mechanism underlying the unique texture formation, the thermal gradient, solidification rate, and migration direction of the liquid-solid interface were numerically analyzed based on a thermal diffusion calculation. The unique CLM was considered for further improvement of the mechanical performance with an approach in which the fabrication direction and the resultant tensile loading axis were tilted by 35° and 45° with respect to the BD, which was determined based on the combination of operative slip systems between the main layer and sub-layer. Finally, the tensile strength was discussed with regard to the contribution of strengthening mechanisms such as the stress-transfer coefficient, crystallographic texture, Hall–Petch relation, and direction of the grain elongation.

2. Experimental method

2.1. Fabrication of IN718 specimens

An Inconel718 spherical powder with size distribution of D10, D50, and D90 were 18.6, 32.3, 57.9 μm, respectively, obtained through gas atomization was used as the starting material. LPBF fabrication of IN718 was conducted using an EOS M290 printer equipped with a 400 W Yb-fiber laser. The building stage was preheated to 80°C to avoid unexpected temperature changes owing to the laser energy input during fabrication to maintain a constant fabrication condition. The building chamber was filled with high-purity argon gas to maintain an oxygen content of below 100 ppm. A meander scan strategy with scan lines spanning the entire 10-mm length (Supp. Fig. S1) was used to fabricate specimens with a height of 15 mm for microstructure observations and a height of 30 mm for the tensile tests, and a bidirectional laser scanning in the x-direction was applied between adjacent layers (Fig. 1(a)) to promote the crystallographic texture formation with sufficient intensity [10,26,28,33].

The process parameters for the fabrication of the IN718 specimens included a fixed layer thickness (h) and hatch spacing (d) of 0.040 mm and 0.080 mm, respectively. The laser power (P) and scan speed (v) were varied within the range of 180–360 W and 600–1400 mm/s, respectively. The volumetric laser energy density (E [J/mm^3]) of the fabrication conditions is defined by Eq. (1) [34]:

$$E = \frac{P}{vhd} \tag{1}$$

2.2. Microstructure characterization

The specimens were cut from the substrate using electrical discharge machining to observe the y-z plane perpendicular to the laser scanning direction. The specimens for microstructural observations were cut at a distance of 5 mm from the 316L substrate, considering the influence of the substrate on the chemical composition of IN718 at the initial stage of fabrication. To observe the microstructure of the specimen, the y-z plane was mechanically polished using up to 4000-grade emery paper and then chemically polished using colloidal silica for mirror-polished surfaces.

Electron backscatter diffraction (EBSD) measurements were conducted using a field-emission scanning electron microscope (FE-SEM; JEOL JIB-4610F, Japan) equipped with EBSD detector (Aztec HKL, Oxford Instruments, UK) under an accelerating voltage of 20 kV and a step interval of 2 μm. The data obtained were analyzed using analysis software (HKL Channel5, Oxford Instruments, UK) to obtain inverse pole figure (IPF) maps and the corresponding pole figures.

To examine the melt pool shape, the mirror-polished surface was further etched in a mixed solution of 31% HNO_3, 6% HF, and

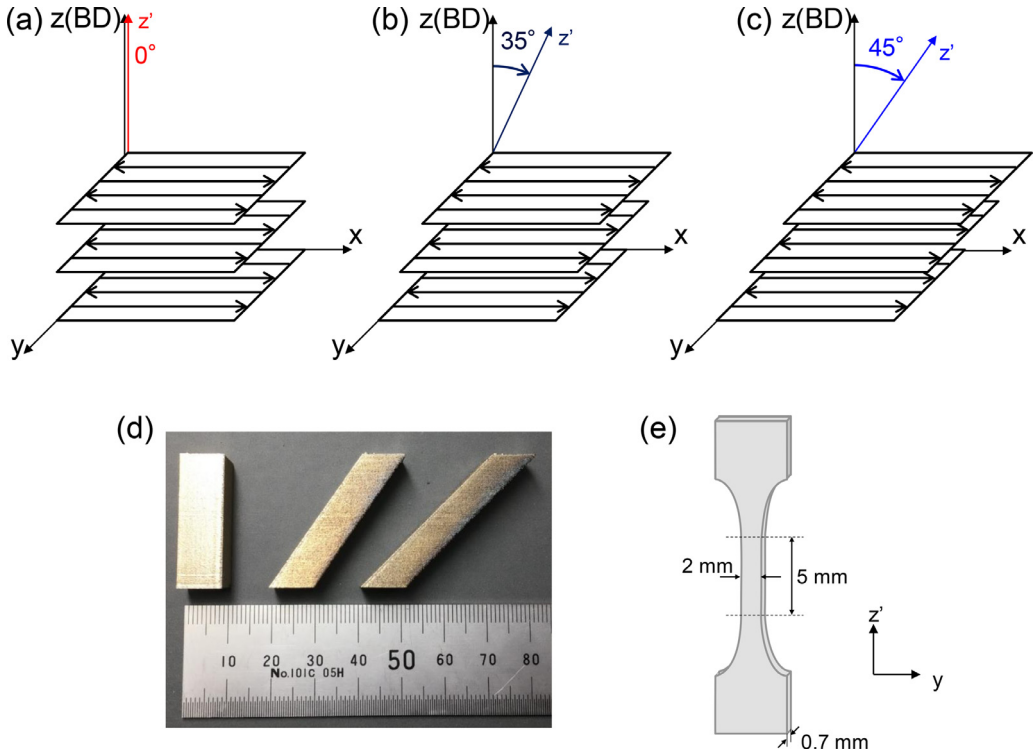

Fig. 1. Schematic representation of the scan strategy for (a) non-tilted, (b) 35° tilted, and (c) 45° tilted fabrication conditions, (d) the corresponding final products, and (e) configuration of tensile specimen.

63% H_2O, soaked for 20 min, immediately washed with water followed by ethanol, and sufficiently dried, and the shape of the melt pool was then investigated using optical microscopy (OM; BX60, Olympus, Japan) and an FE-SEM. For certain conditions, to quantify the observed melt pool shape, the coordinates of the shape were obtained using Image J and then approximated using a cubic function to determine the melt pool shape to calculate the curvature at the bottom of the melt pool.

2.3. Numerical simulation of thermal diffusion

To study the formation mechanism of microstructure under the LPBF, a thermal diffusion analysis was conducted using the finite element (FE) method, and the temperature distribution inside the melt pool and the melt pool shape based on the thermal distribution were analyzed using the simulation software COMSOL Multiphysics™ 5.5. The simulations were carried out under the LPBF conditions for three distinctive textures, CLM (P = 360 W, v = 1000 mm/s), SCM (P = 360 W, v = 1400 mm/s), and PCM (P = 180 W, v = 1400 mm/s).

The simulation model for the laser beam–matter interaction is based on the heat-transfer module of COMSOL Multiphysics. The heat-transfer equation of the fluid was defined through a domain simulation using Eq. (2):

$$\rho C_p\left(\frac{\partial T}{\partial t} + u \cdot \nabla T\right) - \nabla \cdot [k(T)\nabla T] = Q \tag{2}$$

where ρ [kg/m^3], C_p [J/kg·K], and k [W/(m·K)] are the density, effective heat capacity, and thermal conductivity of the fluid, respectively, describing the formation of the temperature field T [K] owing to the energy input by the laser.

In Eq. (2), Q refers to the total energy absorbed by the material from the laser. The simplest form of the FEM simulation of the LPBF process is the surface energy flux absorption model, in which Gaussian heat flux is deposited on the top surface, eliminating the consideration of the particle size, powder packing, and layer thickness. It has been reported that the amount of heat absorbed in a powder bed induced by laser irradiation in AM is approximately 60% owing to the influence of a multiple reflection [35]. It can therefore be expressed mathematically using the following Gaussian distribution determined through Eq. (3).

$$Q_0 = \frac{\alpha P}{\pi R^3 d}\exp\left(-\frac{r^2}{R^2}\right) \times \left(1 - \frac{z}{d}\right)(z < z_0) \tag{3}$$

where P is the laser power, R is the laser beam radius, d is the heat penetration depth, and r is the instantaneous laser beam location. α is powder absorption rate and set to 0.6. d was adjusted based on the melt pool depth [36] using the laser conditions of P = 360 W and v = 1000 mm/s, and this value was considered the same for the other two conditions to compare the thermal behavior in a melt pool. From the numerical results obtained, an in-depth analysis of the melt-pool profile, temperature distribution, and cooling rate will be conducted. The cooling rate represented by $|dT/dt|$ [K/s] as a combined effect of the temperature gradient (G) and solidification rate (R) is analyzed in the discussion section.

The physical properties of IN718, such as thermal conductivity k [W/(m·K)] and heat capacity C_p [J/kg·K], differ depending on the temperature range [37]. Thus, the material data of IN718 built into COMSOL were used, the physical properties of which were set to change depending on the temperature.

2.4. Fabrication of tensile test pieces and tensile test

Rectangular shaped IN718 specimens (10 × 10 × 30 mm^3) were fabricated vertically using LPBF with the process parameters forming CLM, SCM, and PCM. For CLM with the lamellar microstructure, in addition to the vertically fabricated specimen (Fig. 1(a)), 35° angled tensile specimens (35° from the z axis in the x-z plane, as shown in (Fig. 1(b)), 45° angled tensile specimens (45° from the z axis in the x-z plane, as shown in (Fig. 1(c)) were fabricated. The

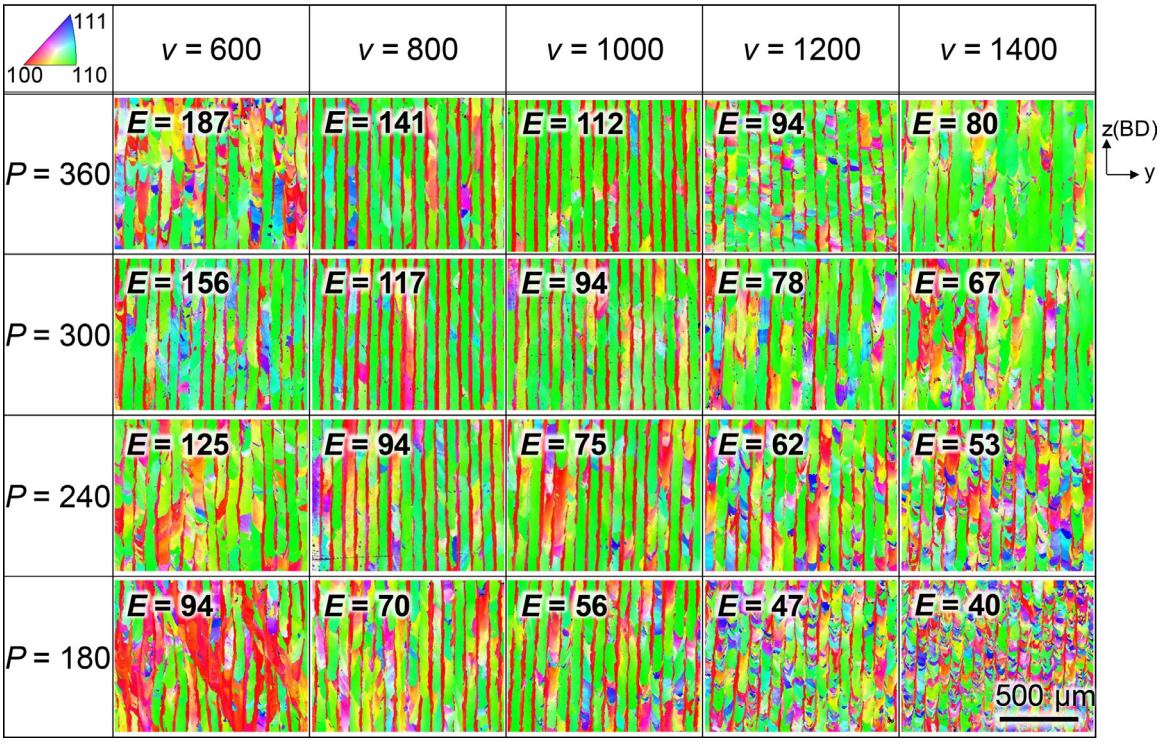

Fig. 2. IPF maps showing the variation in crystallographic texture projected along the build direction (BD) for varied laser power (P [W]) and laser scan speed (v [mm/s]). The laser energy density (E [J/mm^3]) is also presented.

appearance of the specimens is shown in Fig. 1(d). The specimens were separated from the base plate through electrical discharge machining and machined into tensile testing specimens (Fig. 1(e)).

Tensile tests were conducted in a vacuum at room temperature with an initial strain rate of 1.67×10^{-4} s^{-1}. The test was conducted three times for each condition, and the results were averaged. The fracture surfaces were examined using the FE-SEM.

3. Results

3.1. Variations in crystal orientation with process parameter control

Fig. 2 shows the IPF maps of IN718 fabricated with varied laser power (P) and scanning speed (v). The analysis was performed on the y-z plane which is perpendicular to the scan direction, and crystallographic orientation in the BD (z-direction) was projected. The IPF maps in which the orientation was projected in x- and y-directions are shown in Supp. Figs. S2 and S3, respectively. The corresponding {100} pole figures are represented in Fig. 3. In a wide range of the laser conditions, lamellar-type microstructure in which <110>//BD-oriented main layer and <100>//BD-oriented sub-layer stacked in y-direction evolved, which is so-called CLM [25]. The miner spots in the {100} pole figure (see yellow arrows in Fig. 3 at P = 360 W, v = 1000 mm/s) also indicated the evolution of aforementioned CLM. At the condition of P = 360 W and v = 1400 mm/s, the minor pole weakened, indicating the formation of SCM. When fabricated with a lower laser power and higher scan speed, the texture intensity decreased and a polycrystalline-like microstructure (PCM) was obtained.

According to these observations, three characteristics of texture formation can be mentioned, which exhibited a crystallographic lamellar microstructure (CLM, representatively at P = 360 W, v = 1000 mm/s), single-crystal-like microstructure (SCM, P = 360 W, v = 1400 mm/s), and polycrystalline-like microstructure (PCM, representatively at P = 180 W, v = 1400 mm/s). Further examination of the crystallographic texture formation, which was related to the melt pool shape and thermal diffusion behavior of the melt pools, focused on these characteristic textures.

3.2. Crystallographic texture formation mechanism

To understand the relationship between the microstructure including crystallographic texture and melt pool shape, SEM micrographs and IPF maps of the CLM, SCM, and PCM specimens were recorded within the same region (Fig. 4). SEM micrographs represented that highly dense specimens without significant pores were successfully fabricated. Throughout the cross-section, a cellular microstructure was observed (Fig. 5(a-c)). By comparing the SEM images (Fig. 5(a-c)) and the IPF maps (Fig. 5(a'-c')), it can be seen that the cell elongation direction almost agrees with the crystallographic <100> direction. The arrows in the SEM images indicate the direction of cell elongation, as well as <100>. In the CLM and SCM specimens, columnar grains that contain cellular microstructure with identical directionalities and thus crystallographic orientation grew across the multiple melt pools, indicating the occurrence of epitaxial growth. The crystal orientation of the SCM specimen followed the development of <100> oriented cells in each half of the melt pool with ±45° to the BD (green arrows), which produced <110> a single-crystal-like cubic texture accompanied by low-energy low-angle boundaries at the center of the melt pool (Fig. 4(b)). A <110>//BD-oriented single-crystal-like texture formation with ±45° cell growth was previously reported for different Ni-based alloys [33]. However, to the best of our knowledge, this is the first report for IN718 with <110>//BD-oriented single-crystal-like texture. Similarly, in the CLM specimen, the <100> oriented cells angled ±45° with respect to the BD grew from the sidewalls of the melt pool, which formed the <110>//BD texture (Fig. 4(a)). However, in addition to the <110>//BD orientation, <100>//BD-oriented cells developed from the bottom of the melt pool (red arrows), resulting in lamellar-like structure in which two types of

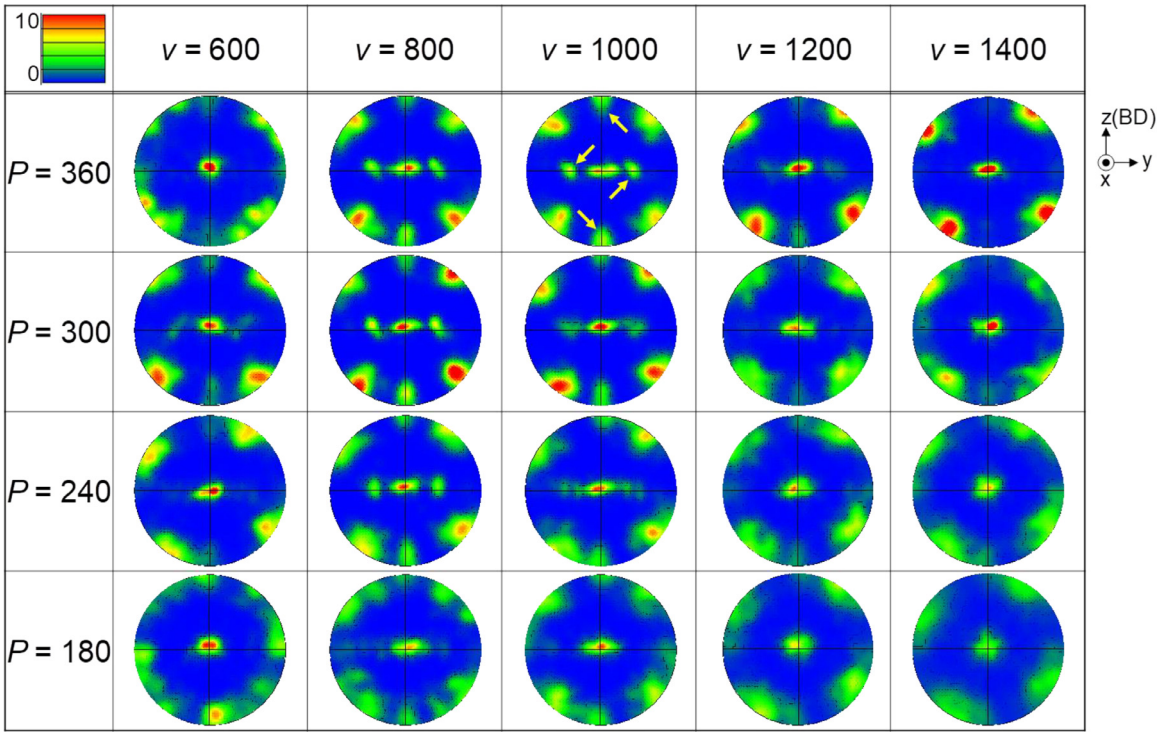

Fig. 3. {100} Pole figures corresponding to crystal orientation maps in Fig. 2.

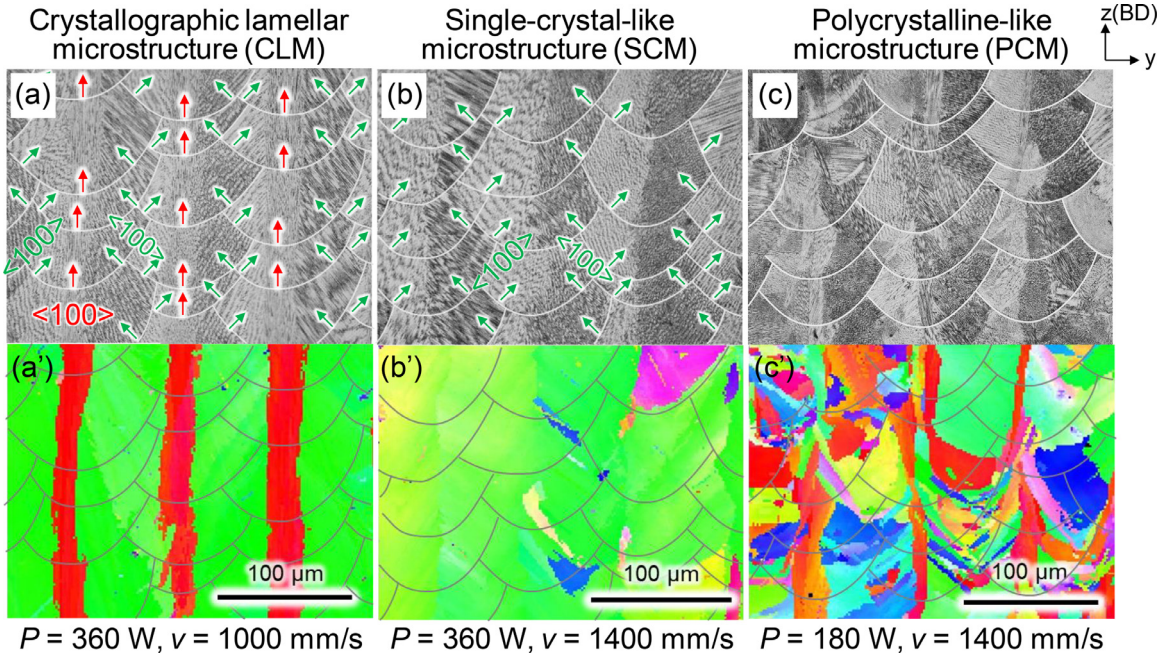

Fig. 4. (a-c) SEM images and (a'-c') IPF maps taken in the same area.

layers with different orientations were alternatively stacked. The periodicity of the lamellar structure coincides with the laser hatching distance (0.080 mm), which can be formed using LPBF but not by other processing techniques. For the PCM condition, the orientation was observably randomized while maintaining the texture to a certain extent, similar to SCM.

To examine the shape of the melt pool without the influence of intrinsic thermal cycles and remelting, and to discuss the cause of such cell growth and the differences between CLM and SCM, the top layers of the CLM and SCM specimens were observed. Fig. 5 shows the IPF maps and corresponding SEM micrographs with the cell orientations on the top layer. The aforementioned characteristics of CLM and SCM with lamellar and single-crystal-like microstructures were carried onto the top layer. The shape of the melt pool differed; the melt pool of the CLM was deeper compared to that of the SCM specimen. The heat-flow direction and shape of the melt pool based on the temperature distribution in the melt pool were analyzed from the thermal diffusion analysis (see Supp. Fig. S4) using the laser conditions for the formation of CLM and SCM, as shown in Fig. 5(c, g). The angle of the heat-flow direction from the melt pool with respect to the BD is displayed in the color regions, as shown using the color scale bar. According

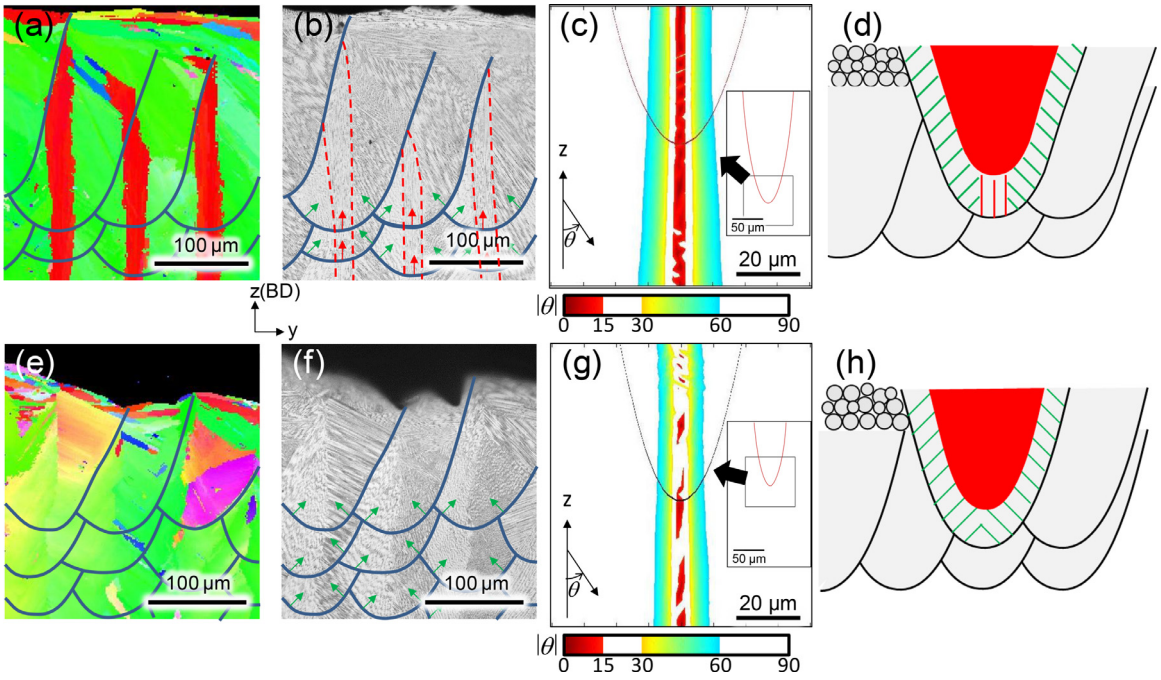

Fig. 5. (a, e) IPF maps and (b, f) the corresponding SEM micrographs of CLM and SCM specimens. The angle of simulated heat flow direction around the melt pool bottom for (c) CLM and (g) SCM with (d, h) representative schematic illustrations of the melt pool formation.

to the simulation of the CLM, the temperature gradient at the bottom of the melt pool was adequately aligned with the BD, which indicates that the normal direction of the solid–liquid interface and the heat-flow direction were approximately the same. For the SCM, by contrast, the direction of the heat-flow at the melt pool bottom tended to be unstable and fluctuating. Schematic illustrations of the melt pools with the cell growth directions according to the microscopic observations and numerical analysis are shown in Fig. 5(d, h).

3.3. Tensile deformation behavior depending on crystallographic texture

Fig. 6(a) shows the tensile true stress–true strain curves of the CLM, SCM, and PCM specimens loaded along the BD. Fig. 6(b) compares the yield stress, ultimate tensile strength (UTS), and elongation. The yield stress was in order of 652±8 MPa for the PCM, 571±3 MPa for the CLM, and 557±7 MPa for the SCM (Table 1). The UTS showed the similar tendency. For the elongation, the order changed as CLM, SCM > PCM. The advantage of the CLM was the preferable balance between relatively high strength and good elongation; therefore, the CLM, unique structure created by the LPBF process, can be proposed to overcome the trade-off between strength and ductility, which has been a long-standing problem in materials science. The LPBF-built specimen showed comparable or superior mechanical properties to the cast material (post-heat treated) [38] even without heat treatment.

The average grain sizes of the CLM, SCM, and PCM, which varied depending on the microstructure of the specimens, is shown in Table 1. To further investigate the grain distribution and grain alignment, the grain size distribution map of the CLM, SCM, and PCM with the red lines corresponding to high-angle grain boundaries (HAGB) are presented in Fig. 7 according to the grain area measurement. PCM grains with an average size of 16.4 μm were found to contain more small grains and fewer large grains than the other CLM and SCM specimens, which correlates with the results of the IPF orientation maps (Fig. 2). In contrast, the grains in the CLM and SCM were large and elongated along the BD with average grain sizes of 24.2 and 21.2, respectively. The grain size distribution and elongation of the specimens with different crystallographic orientations must be considered according to the Hall–Petch equation. Although the Hall–Petch relation predicts that, as the grain size decreases the yield strength increases, it was recently reported that a strong texture formation can alter this relation [39]. Although the grain size of the CLM increased compared to that of the SCM, the yield strength of the CLM was higher along the BD, which also corresponds to the alignment directions of the grains. The PCM with a smaller grain size and increased yield strength agreed with the Hall–Petch relation.

CLM specimens with larger grains exhibited the improved yield stress and UTS compared to the SCM specimens, both of which demonstrated a substantially similar grain alignment along the BD (tensile direction). This result contradicted the Hall–Petch relation, requiring other considerations related to the difference in the

Table 1
Mechanical properties and the related indices of LPBF-built specimens varying with crystallographic orientations.

	Yield strength (MPa)	UTS (MPa)	Elongation (%)	Theoretical SF	Measured SF	Taylor factor	Average grain size (μm)	Stress transfer coefficient
CLM	571 ± 3 [b,c]	1012 ± 24	23.5 ± 2.8 [c]	0.408	0.448	3.41	24.2	0.819
SCM	557 ± 7 [a,c]	957 ± 16 [c]	20.2 ± 0.2 [c]	0.408	0.457	3.23	21.1	1
PCM	652 ± 8 [a,b]	1032 ± 28 [b]	11.6 ± 1.1 [a,b]	-	0.456	3.00	16.4	-
Cast [38]*	651	909	10.3	-	-	-	-	-

SF: Schmid factor.
a: $P < 0.05$ vs CLM, b: $P < 0.05$ vs SCM, c: $P < 0.05$ vs PCM.
* with (homogenization + solution + aging) heat treatments.

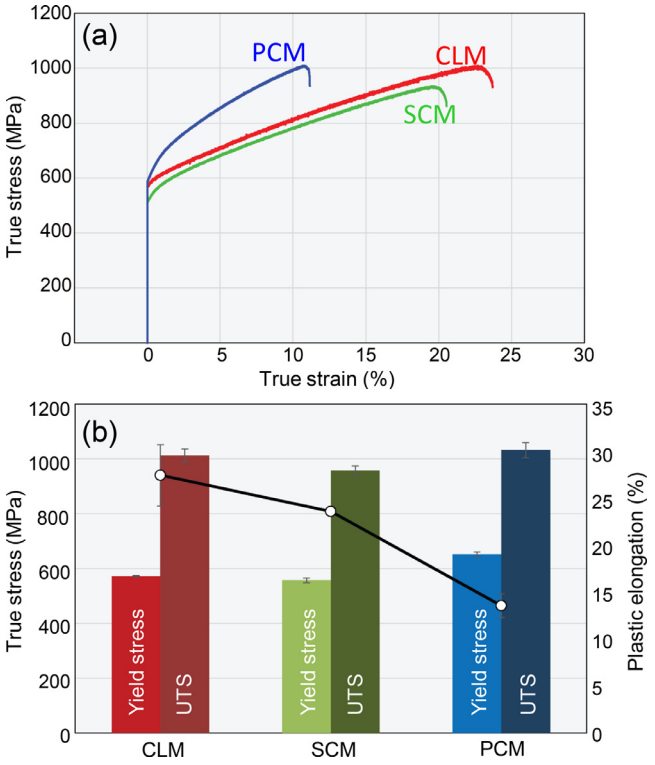

Fig. 6. (a) Tensile true stress–true strain curves of CLM, SCM, and PCM specimens, and (b) quantified yield stress, UTS, and plastic elongation of each condition.

microstructure and/or crystal orientation and its effect on the mechanical properties.

The theoretical Schmid factor for CLM with <110>//BD and <100>//BD orientations and SCM with <110>//BD orientation was 0.408. The measured average Schmid factor of the CLM was slightly lower than that of the SCM (Table 1). The CRSS was calculated to be 227 MPa from the SCM results. In addition to the Schmid factor, the flow stress of polycrystalline metals is usually described using the Taylor formula, where a Taylor factor indicates the resistance to plastic deformation. The grains requiring large amounts of slip systems to consume large plastic deformations show large Taylor factors, which is a slight increase in the Taylor factor of the CLM compared to that of the SCM, corresponding to the trend in the Schmid factor for improving the mechanical strength. Although a difference in the experimental Schmid/Taylor factors between the CLM and SCM was observed, the simultaneously enhanced strength and ductility of the CLM, which has a lamellar microstructure, requires further consideration regarding the difference in the microstructure characteristics compared to the SCM microstructure.

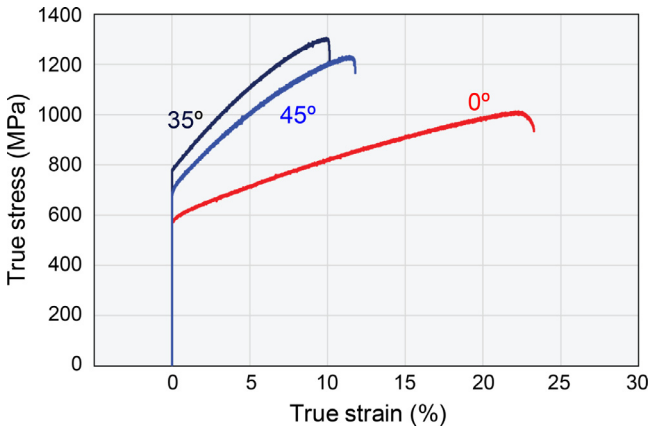

Fig. 8. Tensile true stress–true strain curves of non-tilted (0°), 35° tilted, and 45° tilted-CLM specimens.

3.4. Tensile deformation behavior of CLM depending on the loading axis

To control mechanical properties by utilizing the interface (crystallographic grain boundary) between the main layer and sub-layer, tensile loading axis was varied as described in Fig. 1 to alter the geometric relationship between slip systems in the main and sub-grains and grain boundary, that is, a stress transfer coefficient. In the crystallographic relationship between the main layer and sub-layer evolved in this study, tilt angles less than 35° and between 35° and 45° do not change the stress transfer coefficient, whereas those between 45° and 90° represent identical stress transfer coefficient changes from 45° to 0°; therefore, we selected tilt angles of 0°, 35°, and 45° for the tensile tests. As a result of tilt, loading axis and accordingly Schmid factor were changed (Table 2). The resultant loading axes for the main layer were near <111> for 35° tilt and $<\sqrt{2}11>$ for 45° tilt. Those for the sub-layer were <211> for 35° tilt and $<\sqrt{2}11>$ for 45° tilt. To calculate averaged Schmid factor across the CLM specimen, the proportion of the main and sub-layers was analyzed using ImageJ software, and was determined to be approximately 7:3. Therefore, the averaged Schmid factor was calculated as 0.7 × (Schmid factor for main layer) + 0.3 × (Schmid factor for sub-layer) (Table 2).

Fig. 8 shows the tensile true stress–true strain curves of the CLM specimens fabricated with tilt by 0° (vertical), 35°, and 45°. The yield stress, UTS, and elongation demonstrated dependence on the tilt angle, representing an anisotropy in tensile properties. Table 3 summarizes mechanical properties of the tilted CLM specimens. The calculated yield stress was derived by dividing CRSS obtained from SLM by theoretical Schmid factor, indicating an expected yield stress when the effect of interface between main and

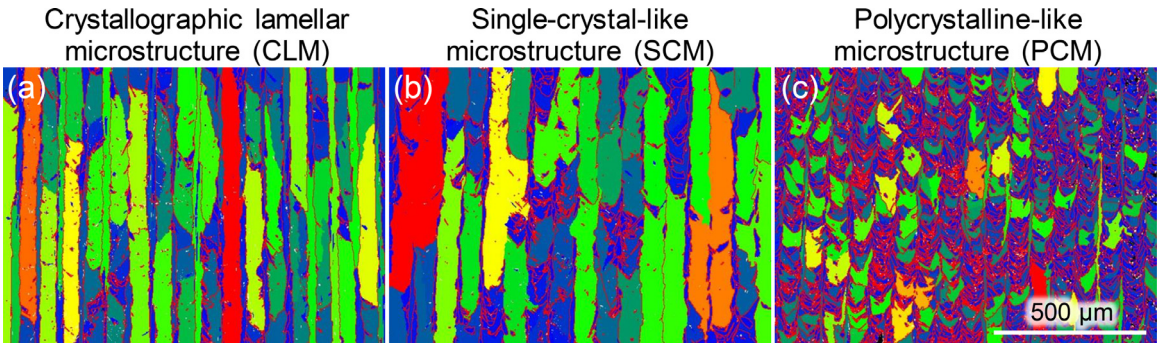

Fig. 7. Grain size maps with HAGB in red color representing the frequency of elongated grains and grain boundaries parallel to the tensile direction.

Table 2
Theoretical and measured Schmid factors of the tilted-CLM specimens for {111}<110> slip system and corresponding Taylor factors, average grain sizes, and stress transmission coefficients.

	Main layer	Sub-layer	Theoretical SF ($0.7SF_{main} + 0.3SF_{sub}$)	Experimental		Average grain size (μm)	Stress transfer coefficient
	Max SF	Max SF		Measured SF	Taylor factor		
0°	0.408	0.408	0.408	0.448	3.29	24.2	0.819
35°	0.275	0.410	0.316	0.377	3.40	32.5	0.652
45°	0.348	0.348	0.348	0.393	3.39	27.4	0.652

SF: Schmid factor.

Table 3
Mechanical properties in between tilted-CLM specimens and calculated yield stress.

Experimental yield stress (MPa)		UTS (MPa)	Elongation (%)	Calculated yield stress (MPa)
0°	571 ± 3 [b,c]	1012 ± 24 [b,c]	23.5 ± 2.8 [b,c]	557
35°	782 ± 5 [a,c]	1287 ± 16 [a]	10.3 ± 0.1 [a,c]	719
45°	740 ± 19 [a,b]	1238 ± 22 [a]	11.9 ± 0.6 [a,b]	653

a: $P < 0.05$ vs 0°, b: $P < 0.05$ vs 35°, c: $P < 0.05$ vs 45°.

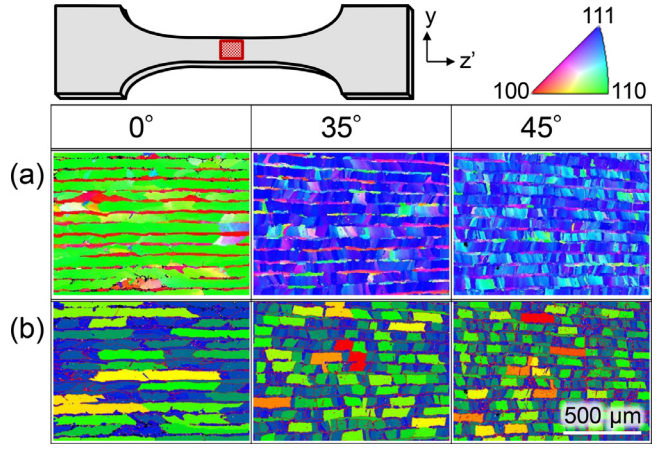

Fig. 9. (a) IPF maps showing the variation in crystallographic orientation parallel to the tensile direction and (b) grain size maps with HAGB in red color representing the frequency of elongated grains and the grain boundaries parallel to the tensile direction.

sub-layers is not taken account. For all specimens, the measured yield stress was higher than the calculated one. The 35° tilt specimen showed the highest yield stress and UTS, and the lowest elongation. Interestingly, the same tendency of the grain size and the mechanical property relationship of the CLM and SCM, where the CLM with a higher grain size demonstrated an enhanced strength and ductility compared to the SCM with a smaller grain size, which is contradictory to the Hall–Petch relation, was observed in the tilted specimens in which the crystallographic orientations were altered. Therefore, these consistent results increased the importance of the possible effect of the crystallographic orientation on the Hall–Petch relation. It is also worth considering the effect of the HAGB alignment with respect to the tensile direction, in which the tilted-CLM conditions exhibited an HAGB formation perpendicular to the tensile load direction, as shown in Fig. 9.

To compare the fracture mechanisms for CLM, SCM, and PCM specimens and CLM specimens tested at different tilt angles, the fracture surface was observed using SEM (Supp. Fig. S5). The final failure can be assumed to have occurred in a ductile manner, as evidenced by a dimpled pattern, which is similar to the previous report of LPBF-fabricated IN718 [31]. In the CLM-0° and SCM specimens, the dimple size is relatively large, unlike CLM-35°, CLM-45°, and PCM specimens that show smaller dimple sizes. It has been reported that the dimple size decreases with a decrease in the elongation [40], which explains the variation in the dimple size observed.

4. Discussion

4.1. Origin of variation in crystal orientation

LPBF-fabricated IN718 specimens showed unique lamellar type crystallographic texture with <110>//BD-oriented main and <100>//BD-oriented sub-layers under a bidirectional scanning strategy only along x direction. By changing the laser power and laser scan speed, the texture could be changed to the single-crystal-like or poly-crystal-like microstructures. This report on changes in crystallographic texture under a wide range of fabrication conditions is valuable.

This transition of the microstructure might be related to the solid–liquid interface, which is mainly affected by constitutional supercooling, which is determined by the ratio of the thermal gradient (G) and the migration velocity of the solid–liquid interface (R) [41]. With the decrease in G/R, planar, cellular, columnar dendritic, and equiaxed dendritic structures are expected to form in sequence. It has been reported that R increases with an increase in the scanning speed or a decrease in the laser power [42,43], and the thermal diffusion simulations in this study correlate with this statement (Table 4). It can be seen that the simulated R values drastically decreased with an increase in laser power, whereas G increased, which indicates an increase in G/R. Thus, strong CLM or SCM formed under the fabrication with higher power. The numerical simulations confirmed that the PCM formed under the condition with lower G/R, forming a mix of columnar and equiaxed grains (Supp. Fig. S6).

A further increase in the laser energy input owing to a decrease in the laser scan speed promoted the transition of the SCM to the CLM (Fig. 4). In the case of the CLM formation, G increased and R decreased, increasing the G/R, which suggested a stronger columnar structure formation than the SCM. Moreover, the melt pool shape of the CLM is altered owing to the high G/R, which resembles a shallow-type key-hole melt pool contributing to the growth of <100> cells parallel to the BD from the bottom of the melt pool. Although the key-hole melt pool shape is mostly avoided owing to the formation of a gas porosity, in this study, the shallow key-hole type melt pool shape promoted the unique CLM. There has been a debate on the shape of the melt pool controlling the crystallo-

Table 4
Thermal gradient (G) and solidification rate (R) at solid–liquid interface of the bottom of the melt pool obtained by thermal diffusion simulation.

Laser power P (W)		Scan speed v (mm/s)		
		600	1000	1400
360	G (K/m)	7.24×10^6	4.79×10^6	3.72×10^6
	R (m/s)	2.75×10^{-3}	1.02×10^{-1}	6.11×10^{-1}
300	G (K/m)	6.31×10^6	3.72×10^6	2.40×10^6
	R (m/s)	2.86×10^{-2}	1.32×10^{-1}	1.38

graphic orientation of cell growth in the melt pool [41,44]. Utilizing the numerical approach, the melt pool shape reflected the temperature distribution affecting the direction of the thermal gradient and the solid–liquid interface migration (Fig. 5(c, g)). The curvature (r) at the bottom of the melt pool was calculated using Eq. (4) by approximating the melt pool shapes of the CLM and SCM, as observed using an optical microscope with a cubic function.

$$r = \frac{\left(1 + f'(a)^2\right)^{\frac{3}{2}}}{|f''(a)|} \tag{4}$$

The curvatures of the melt pool bottom in the CLM and SCM were 39.5 ± 3.2 μm and 31.0 ± 3.3 μm ($P < 0.05$), respectively. This indicates that the melt pool bottom was horizontal and the thermal gradient direction could be aligned in the BD in the CLM. According to the simulations, the thermal gradient at the melt pool bottom was more stable in the case of CLM (Fig. 5(c)) compared to that in the case of SCM (Fig. 5(g)).

4.2. Strengthening mechanisms

The variation in the solidification conditions influence the grain formation mechanism and result in a crystallographic texture; furthermore, the mechanical properties, yield stress, UTS, and elongation varies. The results of the present study revealed that the strength and ductility of IN718 can be altered through the LPBF process by tailoring unique crystallographic textures, such as CLM and SCM, depending on the variation in the BD related crystallographic orientation. In particular, the lamellar microstructure exhibited a simultaneous enhancement in strength and ductility compared to the single-crystal microstructure.

The variation in the mechanical properties depending on the crystallographic texture and the difference in crystallographic orientation through the BD was due to the accumulation of various strengthening mechanisms. The yield stress (σ_{YS}) of a polycrystalline alloy without deformation and precipitation is expected to be the contributions of the individual strengthening mechanisms, i.e., solid solution strengthening (σ_{ss}), grain boundary strengthening (σ_{GB}), precipitation shear effect (σ_{shear}), and friction stress (σ_i), which can be formulated as shown in Eq. (5) [45]:

$$\sigma_{YS} = \sigma_{ss} + \sigma_{GB} + \sigma_{shear} + \sigma_i \tag{5}$$

Considering these strengthening mechanisms, the solid solution strengthening and friction stress can be excluded when comparing the difference in the strengthening of IN718 in this study owing to the compositional similarity. In addition, precipitation shear stress-related strengthening can be neglected because there was no detectable precipitation in as-built specimen owing to the rapid cooling rate (~10^6 K/s) of the LPBF process, which is consistent with a previous report [4]. The lack of precipitation strengthening for LPBF-built components has been reported for other precipitation strengthening superalloys [46,47]. Thus, grain boundary strengthening should be considered in conjunction with the significant crystallographic texture effect. The effect of grain boundaries on the material strength can be discussed based on the Hall–Petch relationship (Eq. (6)):

$$\sigma_{YS} = \sigma_i + k d_{eff}^{-1/2} \tag{6}$$

where k is a constant and d_{eff} is the effective slip distance for an edge dislocation [45]. According to the Hall–Petch relationship, smaller grains exhibit a higher yield strength owing to the difference in the driving force of the dislocation pile-up through the grain boundaries. In the case of PCM with a lower grain size than the CLM and SCM, the strengthening of the grain boundaries was active and resulted in a higher yield stress and UTS, eventually showing a decrease in elongation (Table 1). However, the simultaneously enhanced strength and ductility of the CLM compared to that of the SCM indicated the necessity of elaborating on the strengthening mechanism of the lamellar microstructure. The improvement in the mechanical properties of the CLM is thought to be related to the strengthening mechanism of (a) the crystallographic orientation and (b) the elongated direction of the grains, (c) the effect of texture on the Hall–Petch relation, and (d) the stress-transfer coefficient at the interface (crystallographic grain boundary) of main and sub-layers.

(a) The anisotropy in the tensile strength and work hardening can be described in terms of the resolved stresses. Because the critical resolve shear stress is calculated with the orientation factor, which is called the Schmid factor, the yield stress of the CLM can be related to the Schmid factor. Although the calculated Schmid factors of the CLM and SCM were 0.408, the measured average Schmid factor of the CLM was slightly lower than that of the SCM. However, in the case of polycrystalline metals, the Taylor factor (M), which is called forest dislocation strengthening, is considered. The Taylor factor of the polycrystalline FCC structure is equal to 3.06. The measured average values of the Taylor factor for the CLM, SCM, and PCM are shown in Table 1. The PCM with a Taylor factor of 3.00 experimentally proved the consideration of the polycrystalline microstructure in this study. Furthermore, the higher Taylor factor of the CLM compared to that of the SCM explained the enhancement of the yield stress of the lamellar microstructure. The Taylor factor maps and the distribution are given in the supplementary information (Supp. Fig. S7). The relation between the <110> texture formation and the increased Taylor factor is discussed in [23]. The advantage of the increase in the Taylor factor is considered to be the twinning-induced enhancement of the strength and ductility of the LBF-fabricated 316L stainless steel with <110> crystal orientation. It has been reported that deformation-induced twinning hardly appears when $M < 2.6$, and the majority of twinned grains are aligned near the <111> orientation [23]. It is accepted that the activation of multiple slip systems and the presence of dislocation pile-ups are necessary to induce twinning during deformation, thus requiring grains with a higher Taylor factor (<111> and <110> oriented grains), resulting in simultaneous improvements in the strength and ductility. Although the FCC has a crystal structure with low stacking fault energy, a dislocation pile-up might be enhanced owing to the residual stress induced by the cyclic heating of the LPBF process. Thus, deformation twinning requires more detailed observations.

(b) The anisotropy of the ductility can be attributed to the difference in grain boundary elongation resulting in different cracking mechanisms [16,44,48]. As shown in Fig. 7, both the CLM and SCM consisted of columnar grains along the tensile direction, although an irregular grain size formation between the columnar grains was observed in the SCM. This indicates a tensile load perpendicular to the grain boundaries, complying with Mode I opening tension [16]; therefore, cracks can propagate [48], leading to the lower ductility of the SCM. By contrast, columnar grains parallel to the tensile load will act to deflect the crack tip openings, indicating an improvement in ductility, in which the CLM showed the advantage of a lamellar structure with an increase in the elongated grain boundary along the tensile direction.

(c) The contradiction between the grain size and strength phenomenon, considering the Hall–Petch relation, can be addressed to the effect of texture on Hall–Petch consideration. Because the effect of texture on the Hall–Petch parameters has rarely been reported in the literature, a recent study focusing on strengthening from the grain boundary reported that even a slight texture affects the strength of the material [45]; thus, the Hall–Petch equation is modified, as shown in Eq. (7), including the Taylor factor as the texture effect.

$$\sigma_{YS} = \frac{\sigma_i}{M} + \frac{k}{M} d_{eff}^{-1/2} \tag{7}$$

Thus, the strong texture demonstrates the decrease in the influence of the Hall–Petch relation on the yield stress.

(d) The unique lamellar microstructure (CLM) compared to a SCM requires a consideration of the difference in slip transfer between the <110>//BD and <100>//BD grains. Livingston and Chalmers [49] introduced the stress-transfer coefficient, indicating the difficulty of a crystal deformation when transmitted to the adjacent crystal through the grain boundary (Supp. Fig. S8). When a plastic deformation occurs without cracking or a grain boundary slip, the continuity at the grain boundary of the adjacent grains must be maintained with equal shear stress values of crystal A (P_i^A) and crystal B (P_j^B) [50]. Thus, the stress-transfer coefficient (N_{ij}) was proposed, as shown in Eq. (8).

$$P_j^B = P_i^A \cdot N_{ij} = P_i^A \cdot [(e_i^A \cdot e_j^B)(g_i^A \cdot g_j^B) + (e_i^A \cdot g_j^B)(e_j^B \cdot g_j^A)] \quad (8)$$

A value of N_{ij} closer to 1 indicates that the shear stress can easily be transferred to the slip system of the adjacent crystal. Therefore, the smaller N_{ij} is, the more resistant the slip transmits through the interface, thereby increasing the strength. The N_{ij} of a single-crystal is considered to be equal to 1. The N_{ij} of the CLM was calculated as 0.819. This indicates the strengthening mechanism of the stress transfer between the <110>//BD and <100>//BD grains, which resulted in improved mechanical properties of the CLM compared to that of the SCM.

To tune the mechanical performances of the CLM products, controlling the volume ratio of main layer and sub-layers and the periodicity of the lamellar structure are promising. The volume ratio could be changed by changing the curvature of the melt pool bottom, as described in Eq. (4), through the laser conditions to change the average Schmid factor. The periodicity of lamellar structure could be changed by changing the scan pitch, leading to a change in the density of the main layer and sub-layer interface, which acts as a disturbance of stress transfer. The introduction of CLM is expected to extend the tunability of the control of the mechanical properties.

In the AM processes, a common approach is to alter the BD to elevate certain material properties, such as the crystallographic orientation and grain alignment [27,48,51]. In this study, the layer-by-layer fabrication was tilted to allow the formation of different crystallographic orientations keeping the loading axis parallel to the lamellar direction. This is because we aim to investigate the effect of stress transfer through the main layer and sub-layer interface to evaluate the contribution of the presence of the interface to the mechanical strength. Therefore, significant mechanical anisotropy was observed (Table 3). The superior yield stress and UTS of the 35° specimen can be attributed to the low Schmid factor with the corresponding Taylor factor and the effect of the stress-transfer coefficient. A similar tendency regarding the grain size, which contradicts the Hall–Petch relation, was observed for the tilted specimens, although the strong texture formation reduces the effect of the Hall–Petch relation in this study. By contrast, vertical grain boundaries along the columnar grains with respect to the build and tensile directions were detected from the tilted-CLM specimens (Fig. 9(b)), which occurred owing to the tilted fabrication conditions. The vertical HAGB in the tensile direction caused a decrease in elongation for the 35° and 45° specimens (Fig. 8). However, the mechanical properties of the CLM with different BD offer an adjustable range of mechanical properties that can be proposed for various industrial applications.

The results obtained in the present study suggest that the LPBF can develop unique microstructures that are not obtained by other processes, and thus have significant potential for developing structural applications for as-built IN718. One challenge regarding the CLM, the characteristic microstructure uniquely obtained by LPBF, is the amelioration of heterogeneity of the lamellar structure along the BD, in order to reduce variability of the mechanical properties and further improve the mechanical reliability.

IN718 is a superalloy used at a high temperature of up to ~650°C after solution and aging heat treatment. In this study, we did not investigate the effects of heat treatment on the specific microstructures and mechanical properties obtained in the as-built condition. Along a standard scheme of heat treatment of IN718, the solution heat treatment at 1080°C for 1 h did not cause significant grain coarsening and recrystallization [52,53]. The CLM was possibly retained after solution heat treatment. In addition, subsequent heat treatments for precipitation strengthening, around 950°C for the δ-phase and 600–750°C for the γ'/γ'' phases, can be added to further improve the mechanical properties. Properly controlled precipitation of these strengthening phases significantly enhances the yield strength [54,55], UTS [54,55], creep strength [54], and fatigue strength [56] at high temperatures, at the expense of elongation to some extent. Future studies are needed to elucidate the effects of the unique microstructures obtained in this study on the high-temperature mechanical behaviors.

To the best of the authors' knowledge, this study is the first to report the enhanced strength and ductility with a lamellar microstructure in IN718. Considering the strengthening mechanisms, the effect of the crystallographic orientation on the mechanical properties was significant. By utilizing the texture control through an altered grain formation mechanism by the LPBF process parameters, the CLM specimens suppressed the mechanical requirements of the cast IN718.

5. Conclusion

In this study, the variation of the LPBF process parameters, that is, the laser speed and laser power, was used to manipulate the microstructure, crystallographic orientation, and mechanical properties of IN718. The combination of experimental observations and numerical simulations facilitated a better fundamental understanding of the correlation between the process, structure, and property relationships. The following conclusions can be drawn:

(1) The variation in the laser condition (laser speed and laser power) exhibited the transition of different characteristic textures, SCM, CLM, and PCM. The laser condition would affect the thermal gradient (G) and solidification rate (R). The PCM evolved under the laser condition with lower G/R.
(2) The formation of the SCM with <110>//BD orientation was first reported in IN718, whereas previous studies focused on the <100> cubic texture. Moreover, to the best of the authors' knowledge, a unique CLM with <110>//BD-oriented main layer and <100>//BD-oriented sub-layer was obtained for the first time in IN718.
(3) The formation of SCM or CLM could be explained by the flatness (radius of curvature) of the melt pool bottom. The flatter melt pool bottom shape provided a more stable heat flow and solid-liquid interface migration along BD at the bottom of the melt pool, producing <100>//BD-oriented grains at the center of the melt pool, resulting in the lamellar microstructure (CLM).
(4) Different strengthening mechanisms contributed to the yield stress of the specimens. The mechanical properties of the PCM followed the Hall–Petch relation; however, the Hall–Petch relation was ineffective in explaining the SCM and CLM with strong textures.
(5) The strong crystallographic orientation in the CLM and SCM activated a texture-related strengthening mechanism; in addition, the Schmid factor, Taylor factor, and stress-transfer coefficient were revealed as the strongest contributors to the strengthening, followed by the grain boundary orientation.

Especially in CLM, the introduction of the crystallographic interface moderately lowered the stress-transfer coefficient and thus increased the resistance to slip transmission, resulting in the increased yield stress.

The findings of the present study will be of significance in additively manufacturing other types of metallic materials into high-performance parts without a secondary heat treatment process. This study highlights the importance of certain crystallographic texture formations and its effect on the mechanical properties, showing that the mechanical properties of IN718 can be improved with texture control. Engineering of the crystallographic textures in a microstructure using the rapid solidification characteristics of the LPBF process is a promising method to overcome the long-lasting strength–ductility dilemma in metallic materials. Therefore, this is a promising approach to producing metallic components with enhanced strength and ductility for future industrial use.

Declaration of Competing Interest

The authors declare that they have no known competing financial interests or personal relationships that could have appeared to influence the work reported in this paper.

CRediT authorship contribution statement

Ozkan Gokcekaya: Data curation, Investigation, Validation, Visualization, Writing - original draft. **Takuya Ishimoto:** Investigation, Methodology, Writing - review & editing. **Shinya Hibino:** Investigation, Methodology. **Jumpei Yasutomi:** Formal analysis, Investigation, Methodology, Visualization. **Takayuki Narushima:** Writing - review & editing. **Takayoshi Nakano:** Conceptualization, Project administration, Supervision, Writing - review & editing.

Acknowledgments

This work was supported by Grants-in-Aid for Scientific Research (JP18H05254) from the Japan Society for the Promotion of Science (JSPS). This work was also partly supported by the Cross-Ministerial Strategic Innovation Promotion Program (SIP), –Materials Integration for Revolutionary Design System of Structural Materials–, Domain C1: “Development of Additive Manufacturing Process for Ni-based Alloy” from the Japan Science and Technology Agency (JST).

Supplementary materials

Supplementary material associated with this article can be found, in the online version, at doi:10.1016/j.actamat.2021.116876.

References

[1] T.S. Srivatsan, T.S. Sudarshan, Additive Manufacturing: Innovations, Advances, and Applications, CRC Press, 2015.
[2] D. Carluccio, A.G. Demir, M.J. Bermingham, M.S. Dargusch, Challenges and Opportunities in the Selective Laser Melting of Biodegradable Metals for Load-Bearing Bone Scaffold Applications, Metall. Mater. Trans. A. 51 (2020) 3311–3334, doi:10.1007/s11661-020-05796-z.
[3] O. Gokcekaya, N. Hayashi, T. Ishimoto, K. Ueda, T. Narushima, T. Nakano, Crystallographic orientation control of pure chromium via laser powder-bed fusion and improved high temperature oxidation resistance, Addit. Manuf. (2020), doi:10.1016/j.addma.2020.101624.
[4] Z. Sun, X. Tan, S.B. Tor, W.Y. Yeong, Selective laser melting of stainless steel 316L with low porosity and high build rates, Mater. Des. 104 (2016) 197–204, doi:10.1016/j.matdes.2016.05.035.
[5] B. Zhang, H. Liao, C. Coddet, Effects of processing parameters on properties of selective laser melting Mg–9%Al powder mixture, Mater. Des. 34 (2012) 753–758, doi:10.1016/j.matdes.2011.06.061.
[6] A. Yadollahi, N. Shamsaei, S.M. Thompson, A. Elwany, L. Bian, Effects of building orientation and heat treatment on fatigue behavior of selective laser melted 17-4 PH stainless steel, Int. J. Fatigue. 94 (2017) 218–235, doi:10.1016/j.ijfatigue.2016.03.014.
[7] C.Y. Yap, C.K. Chua, Z.L. Dong, Z.H. Liu, D.Q. Zhang, L.E. Loh, S.L. Sing, Review of selective laser melting: Materials and applications, Appl. Phys. Rev. 2 (2015) 41101, doi:10.1063/1.4935926.
[8] J.A. Cherry, H.M. Davies, S. Mehmood, N.P. Lavery, S.G.R. Brown, J. Sienz, Investigation into the effect of process parameters on microstructural and physical properties of 316L stainless steel parts by selective laser melting, Int. J. Adv. Manuf. Technol. 76 (2015) 869–879, doi:10.1007/s00170-014-6297-2.
[9] L.N. Carter, C. Martin, P.J. Withers, M.M. Attallah, The influence of the laser scan strategy on grain structure and cracking behaviour in SLM powder-bed fabricated nickel superalloy, J. Alloys Compd. 615 (2014) 338–347, doi:10.1016/j.jallcom.2014.06.172.
[10] T. Ishimoto, K. Hagihara, K. Hisamoto, S.-H. Sun, T. Nakano, Crystallographic texture control of beta-type Ti–15Mo–5Zr–3Al alloy by selective laser melting for the development of novel implants with a biocompatible low Young's modulus, Scr. Mater. 132 (2017) 34–38, doi:10.1016/j.scriptamat.2016.12.038.
[11] F. Liu, X. Lin, C. Huang, M. Song, G. Yang, J. Chen, W. Huang, The effect of laser scanning path on microstructures and mechanical properties of laser solid formed nickel-base superalloy Inconel 718, J. Alloys Compd. 509 (2011) 4505–4509, doi:10.1016/j.jallcom.2010.11.176.
[12] R. Rashid, S.H. Masood, D. Ruan, S. Palanisamy, R.A. Rahman Rashid, M. Brandt, Effect of scan strategy on density and metallurgical properties of 17-4PH parts printed by Selective Laser Melting (SLM), J. Mater. Process. Technol. 249 (2017) 502–511, doi:10.1016/j.jmatprotec.2017.06.023.
[13] L. Parry, I.A. Ashcroft, R.D. Wildman, Understanding the effect of laser scan strategy on residual stress in selective laser melting through thermo-mechanical simulation, Addit. Manuf. 12 (2016) 1–15, doi:10.1016/j.addma.2016.05.014.
[14] H.Y. Wan, Z.J. Zhou, C.P. Li, G.F. Chen, G.P. Zhang, Effect of scanning strategy on mechanical properties of selective laser melted Inconel 718, Mater. Sci. Eng. A. 753 (2019) 42–48, doi:10.1016/j.msea.2019.03.007.
[15] Y.C. Wang, L.M. Lei, L. Shi, H.Y. Wan, F. Liang, G.P. Zhang, Scanning strategy dependent tensile properties of selective laser melted GH4169, Mater. Sci. Eng. A. 788 (2020) 139616, doi:10.1016/j.msea.2020.139616.
[16] M. Ni, C. Chen, X. Wang, P. Wang, R. Li, X. Zhang, K. Zhou, Anisotropic tensile behavior of in situ precipitation strengthened Inconel 718 fabricated by additive manufacturing, Mater. Sci. Eng. A. 701 (2017) 344–351, doi:10.1016/j.msea.2017.06.098.
[17] H. Qi, M. Azer, A. Ritter, Studies of standard heat treatment effects on microstructure and mechanical properties of laser net shape manufactured INCONEL 718, Metall. Mater. Trans. A. 40 (2009) 2410–2422, doi:10.1007/s11661-009-9949-3.
[18] K.N. Amato, S.M. Gaytan, L.E. Murr, E. Martinez, P.W. Shindo, J. Hernandez, S. Collins, F. Medina, Microstructures and mechanical behavior of Inconel 718 fabricated by selective laser melting, Acta Mater 60 (2012) 2229–2239, doi:10.1016/j.actamat.2011.12.032.
[19] H.L. Wei, J. Mazumder, T. DebRoy, Evolution of solidification texture during additive manufacturing, Sci. Rep. 5 (2015) 16446, doi:10.1038/srep16446.
[20] M. Gäumann, C. Bezençon, P. Canalis, W. Kurz, Single-crystal laser deposition of superalloys: processing–microstructure maps, Acta Mater 49 (2001) 1051–1062, doi:10.1016/S1359-6454(00)00367-0.
[21] P. Kumar, O. Prakash, U. Ramamurty, Micro-and meso-structures and their influence on mechanical properties of selectively laser melted Ti-6Al-4V, Acta Mater 154 (2018) 246–260, doi:10.1016/j.actamat.2018.05.044.
[22] M. Garibaldi, I. Ashcroft, M. Simonelli, R. Hague, Metallurgy of high-silicon steel parts produced using Selective Laser Melting, Acta Mater 110 (2016) 207–216, doi:10.1016/j.actamat.2016.03.037.
[23] Z. Sun, X. Tan, S.B. Tor, C.K. Chua, Simultaneously enhanced strength and ductility for 3D-printed stainless steel 316L by selective laser melting, NPG Asia Mater 10 (2018) 127–136, doi:10.1038/s41427-018-0018-5.
[24] T.D. McLouth, D.B. Witkin, G.E. Bean, S.D. Sitzman, P.M. Adams, J.R. Lohser, J.-M. Yang, R.J. Zaldivar, Variations in ambient and elevated temperature mechanical behavior of IN718 manufactured by selective laser melting via process parameter control, Mater. Sci. Eng. A. 780 (2020) 139184, doi:10.1016/j.msea.2020.139184.
[25] S.-H. Sun, T. Ishimoto, K. Hagihara, Y. Tsutsumi, T. Hanawa, T. Nakano, Excellent mechanical and corrosion properties of austenitic stainless steel with a unique crystallographic lamellar microstructure via selective laser melting, Scr. Mater. 159 (2019) 89–93, doi:10.1016/j.scriptamat.2018.09.017.
[26] T. Ishimoto, S. Wu, Y. Ito, S.-H. Sun, H. Amano, T. Nakano, Crystallographic orientation control of 316L austenitic stainless steel via selective laser melting, ISIJ Int 60 (2020) 1758–1764, doi:10.2355/isijinternational.ISIJINT-2019-744.
[27] S.-H. Sun, Y. Koizumi, T. Saito, K. Yamanaka, Y.-P. Li, Y. Cui, A. Chiba, Electron beam additive manufacturing of Inconel 718 alloy rods: Impact of build direction on microstructure and high-temperature tensile properties, Addit. Manuf. 23 (2018) 457–470, doi:10.1016/j.addma.2018.08.017.
[28] K. Hagihara, T. Nakano, M. Suzuki, T. Ishimoto, S.-H.Sun Suyalatu, S.-H. Sun, Successful additive manufacturing of $MoSi_2$ including crystallographic texture and shape control, J. Alloys Compd. 696 (2017) 67–72, doi:10.1016/j.jallcom.2016.11.191.
[29] T. Nagase, T. Hori, M. Todai, S.-H. Sun, T. Nakano, Additive manufacturing of dense components in beta-titanium alloys with crystallographic texture from a mixture of pure metallic element powders, Mater. Des. 173 (2019) 107771, doi:10.1016/j.matdes.2019.107771.
[30] Q. Jia, D. Gu, Selective laser melting additive manufacturing of Inconel 718 superalloy parts: Densification, microstructure and properties, J. Alloys Compd. 585 (2014) 713–721, doi:10.1016/j.jallcom.2013.09.171.

[31] V.A. Popovich, E.V Borisov, A.A. Popovich, V.S. Sufiiarov, D.V Masaylo, L. Alzina, Functionally graded Inconel 718 processed by additive manufacturing: Crystallographic texture, anisotropy of microstructure and mechanical properties, Mater. Des. 114 (2017) 441–449, doi:10.1016/j.matdes.2016.10.075.
[32] M.C. Chaturvedi, Y. Han, Strengthening mechanisms in Inconel 718 superalloy, Met. Sci. 17 (1983) 145–149, doi:10.1179/030634583790421032.
[33] S.-H. Sun, K. Hagihara, T. Nakano, Effect of scanning strategy on texture formation in Ni-25at.%Mo alloys fabricated by selective laser melting, Mater. Des. 140 (2018) 307–316, doi:10.1016/j.matdes.2017.11.060.
[34] D. Gu, Y. Shen, Effects of processing parameters on consolidation and microstructure of W–Cu components by DMLS, J. Alloys Compd. 473 (2009) 107–115, doi:10.1016/j.jallcom.2008.05.065.
[35] H.J. Willy, X. Li, Z. Chen, T.S. Herng, S. Chang, C.Y.A. Ong, C. Li, J. Ding, Model of laser energy absorption adjusted to optical measurements with effective use in finite element simulation of selective laser melting, Mater. Des. 157 (2018) 24–34, doi:10.1016/j.matdes.2018.07.029.
[36] A. Foroozmehr, M. Badrossamay, E. Foroozmehr, S. Golabi, Finite element simulation of selective laser melting process considering optical penetration depth of laser in powder bed, Mater. Des. 89 (2016) 255–263, doi:10.1016/j.matdes.2015.10.002.
[37] N. Raghavan, R. Dehoff, S. Pannala, S. Simunovic, M. Kirka, J. Turner, N. Carlson, S.S. Babu, Numerical modeling of heat-transfer and the influence of process parameters on tailoring the grain morphology of IN718 in electron beam additive manufacturing, Acta Mater 112 (2016) 303–314, doi:10.1016/j.actamat.2016.03.063.
[38] D. Zhang, Z. Feng, C. Wang, W. Wang, Z. Liu, W. Niu, Comparison of microstructures and mechanical properties of Inconel 718 alloy processed by selective laser melting and casting, Mater. Sci. Eng. A 724 (2018) 357–367, doi:10.1016/j.msea.2018.03.073.
[39] M.T. Andani, A. Lakshmanan, V. Sundararaghavan, J. Allison, A. Misra, Quantitative study of the effect of grain boundary parameters on the slip system level Hall-Petch slope for basal slip system in Mg-4Al, Acta Mater 200 (2020) 148–161, doi:10.1016/j.actamat.2020.08.079.
[40] S. Ghosh, A.K. Singh, S. Mula, Effect of critical temperatures on microstructures and mechanical properties of Nb–Ti stabilized IF steel processed by multiaxial forging, Mater. Design. 100 (2016) 47–57, doi:10.1016/j.matdes.2016.03.107.
[41] T. DebRoy, H.L. Wei, J.S. Zuback, T. Mukherjee, J.W. Elmer, J.O. Milewski, A.M. Beese, A. Wilson-Heid, A. De, W. Zhang, Additive manufacturing of metallic components – Process, structure and properties, Prog. Mater. Sci. 92 (2018) 112–224, doi:10.1016/j.pmatsci.2017.10.001.
[42] S. Bontha, N.W. Klingbeil, P.A. Kobryn, H.L. Fraser, Effects of process variables and size-scale on solidification microstructure in beam-based fabrication of bulky 3D structures, Mater. Sci. Eng. A. 513–514 (2009) 311–318, doi:10.1016/j.msea.2009.02.019.
[43] P. Promoppatum, S.-C. Yao, P.C. Pistorius, A.D. Rollett, A comprehensive comparison of the analytical and numerical prediction of the thermal history and solidification microstructure of Inconel 718 products made by laser powder-bed fusion, Engineering 3 (2017) 685–694, doi:10.1016/J.ENG.2017.05.023.
[44] P. Köhnen, M. Létang, M. Voshage, J.H. Schleifenbaum, C. Haase, Understanding the process-microstructure correlations for tailoring the mechanical properties of L-PBF produced austenitic advanced high strength steel, Addit. Manuf. 30 (2019) 100914, doi:10.1016/j.addma.2019.100914.
[45] S. Ghorbanpour, M.E. Alam, N.C. Ferreri, A. Kumar, B.A. McWilliams, S.C. Vogel, J. Bicknell, I.J. Beyerlein, M. Knezevic, Experimental characterization and crystal plasticity modeling of anisotropy, tension-compression asymmetry, and texture evolution of additively manufactured Inconel 718 at room and elevated temperatures, Int. J. Plast. 125 (2020) 63–79, doi:10.1016/j.ijplas.2019.09.002.
[46] S.P. Murray, K.M. Pusch, A.T. Polonsky, C.J. Torbet, G.G.E. Seward, N. Zhou, S.A.J. Forsik, P. Nandwana, M.M. Kirka, R.R. Dehoff, W.E. Slye, T.M. Pollock, A defect-resistant Co–Ni superalloy for 3D printing, Nat. Commun. 11 (2020) 4975, doi:10.1038/s41467-020-18775-0.
[47] H. Wu, D. Zhang, B. Yang, C. Chena, Y. Lia, K. Zhou, L. Jiang, R. Liu, Microstructural evolution and defect formation in a powder metallurgy nickel-based superalloy processed by selective laser melting, J. Mater. Sci. Technol. 36 (2020) 7–17, doi:10.1016/j.jmst.2019.08.007.
[48] G.E. Bean, T.D. McLouth, D.B. Witkin, S.D. Sitzman, P.M. Adams, R.J. Zaldivar, Build orientation effects on texture and mechanical properties of selective laser melting Inconel 718, J. Mater. Eng. Perform. 28 (2019) 1942–1949, doi:10.1007/s11665-019-03980-w.
[49] J.D. Livingston, B. Chalmers, Multiple slip in bicrystal deformation, Acta Metall 5 (1957) 322–327, doi:10.1016/0001-6160(57)90044-5.
[50] N.V Malyar, G. Dehm, C. Kirchlechner, Strain rate dependence of the slip transfer through a penetrable high angle grain boundary in copper, Scr. Mater. 138 (2017) 88–91, doi:10.1016/j.scriptamat.2017.05.042.
[51] M. Todai, T. Nakano, T. Liu, H.Y. Yasuda, K. Hagihara, K. Cho, M. Ueda, M. Takeyama, Effect of building direction on the microstructure and tensile properties of Ti-48Al-2Cr-2Nb alloy additively manufactured by electron beam melting, Addit. Manuf. 13 (2017) 61–70, doi:10.1016/j.addma.2016.11.001.
[52] Y. Zhao, Q. Guo, Z. Ma, L. Yu, Comparative study on the microstructure evolution of selective laser melted and wrought IN718 superalloy during subsequent heat treatment process and its effect on mechanical properties, Mater. Sci. Eng. A 791 (2020) 139735, doi:10.1016/j.msea.2020.139735.
[53] E.M. Fayed, M. Saadati, D. Shahriari, V. Brailovski, M. Jahazi, M. Medraj, Effect of homogenization and solution treatments time on the elevated-temperature mechanical behavior of Inconel 718 fabricated by laser powder bed fusion, Sci. Rep. 11 (2021) 2020, doi:10.1038/s41598-021-81618-5.
[54] M. Cao, D. Zhang, Y. Gao, R. Chen, G. Huang, Z. Feng, R. Poprawe, J.H. Schleifenbaum, S. Ziegler, The effect of homogenization temperature on the microstructure and high temperature mechanical performance of SLM-fabricated IN718 alloy, Mater. Sci. Eng. A 801 (2021) 140427, doi:10.1016/j.msea.2020.140427.
[55] X. Li, J.J. Shi, G.H. Cao, A.M. Russell, Z.J. Zhou, C.P. Li, G.F. Chen, Improved plasticity of Inconel 718 superalloy fabricated by selective laser melting through a novel heat treatment process, Mater. Design. 180 (2019) 107915, doi:10.1016/j.matdes.2019.107915.
[56] H.Y Wan, Z.J. Zhou, C.P. Li, G.F. Chen, G.P. Zhang, Enhancing fatigue strength of selective laser melting-fabricated Inconel 718 by tailoring heat treatment route, Adv. Eng. Mater. 20 (2018) 1800307, doi:10.1002/adem.201800307.